Measuring three-dimensional interaction potentials using optical interference

Mojarad, Nassiredin ; Sandoghdar, Vahid ; Krishnan, Madhavi

Abstract: We describe the application of three-dimensional (3D) scattering interferometric (iSCAT) imaging to the measurement of spatial interaction potentials for nano-objects in solution. We study electrostatically trapped gold particles in a nanofluidic device and present details on axial particle localization in the presence of a strongly reflecting interface. Our results demonstrate high-speed (kHz) particle tracking with subnanometer localization precision in the axial and average 2.5 nm in the lateral dimension. A comparison of the measured levitation heights of trapped particles with the calculated values for traps of various geometries reveals good agreement. Our work demonstrates that iSCAT imaging delivers label-free, high-speed and accurate 3D tracking of nano-objects conducive to probing weak and long-range interaction potentials in solution.

DOI: https://doi.org/10.1364/OE.21.009377

Measuring three-dimensional interaction potentials using optical interference

Nassir Mojarad,[1] Vahid Sandoghdar,[2] and Madhavi Krishnan[3,4,*]

[1] *Laboratory for Micro- and Nanotechnology, Paul Scherrer Institut, 5232 Villigen, Switzerland*
[2] *Max Planck Institute for the Science of Light, 91058 Erlangen, Germany*
[3] *Institute of Physical Chemistry, University of Zurich, Winterthurerstrasse 190, 8057 Zürich, Switzerland*
[4] *Institute of Physics, University of Zurich, Winterthurerstrasse 190, 8057 Zürich, Switzerland*
[*] *madhavi.krishnan@uzh.ch*

Abstract: We describe the application of three-dimensional (3D) scattering interferometric (iSCAT) imaging to the measurement of spatial interaction potentials for nano-objects in solution. We study electrostatically trapped gold particles in a nanofluidic device and present details on axial particle localization in the presence of a strongly reflecting interface. Our results demonstrate high-speed (~kHz) particle tracking with subnanometer localization precision in the axial and average 2.5 nm in the lateral dimension. A comparison of the measured levitation heights of trapped particles with the calculated values for traps of various geometries reveals good agreement. Our work demonstrates that iSCAT imaging delivers label-free, high-speed and accurate 3D tracking of nano-objects conducive to probing weak and long-range interaction potentials in solution.

OCIS codes: (110.0180) Microscopy; (110.1650) Coherence imaging; (170.6900) Three-dimensional microscopy; (180.3170) Interference microscopy.

References and links

1. J. N. Israelachvili and G. E. Adams, "Measurement of forces between 2 mica surfaces in aqueous electrolyte solutions in range 0-100 nm," J. Chem. Soc, Faraday Trans. 1 F **74**, 975–1001 (1978).
2. W. A. Ducker, T. J. Senden, and R. M. Pashley, "Direct measurement of colloidal forces using an atomic force microscope," Nature **353**(6341), 239–241 (1991).
3. K. C. Neuman and A. Nagy, "Single-molecule force spectroscopy: optical tweezers, magnetic tweezers and atomic force microscopy," Nat. Methods **5**(6), 491–505 (2008).
4. M. A. Bevan and S. L. Eichmann, "Optical microscopy measurements of kT-scale colloidal interactions," Curr. Opin. Colloid Interface Sci. **16**(2), 149–157 (2011).
5. M. B. Hochrein, J. A. Leierseder, L. Golubović, and J. O. Rädler, "DNA localization and stretching on periodically microstructured lipid membranes," Phys. Rev. Lett. **96**(3), 038103 (2006).
6. M. Krishnan, I. Mönch, and P. Schwille, "Spontaneous stretching of DNA in a two-dimensional nanoslit," Nano Lett. **7**(5), 1270–1275 (2007).
7. M. Polin, D. G. Grier, and Y. Han, "Colloidal electrostatic interactions near a conducting surface," Phys. Rev. E Stat. Nonlin. Soft Matter Phys. **76**(4), 041406 (2007).
8. M. A. Bevan and D. C. Prieve, "Direct measurement of retarded van der Waals attraction," Langmuir **15**(23), 7925–7936 (1999).
9. P. Bahukudumbi and M. A. Bevan, "Imaging energy landscapes with concentrated diffusing colloidal probes," J. Chem. Phys. **126**(24), 244702 (2007).
10. A. D. Dinsmore, D. T. Wong, P. Nelson, and A. G. Yodh, "Hard spheres in vesicles: curvature-induced forces and particle-induced curvature," Phys. Rev. Lett. **80**(2), 409–412 (1998).
11. F. Soyka, O. Zvyagolskaya, C. Hertlein, L. Helden, and C. Bechinger, "Critical Casimir forces in colloidal suspensions on chemically patterned surfaces," Phys. Rev. Lett. **101**(20), 208301 (2008).
12. R. E. Thompson, D. R. Larson, and W. W. Webb, "Precise nanometer localization analysis for individual fluorescent probes," Biophys. J. **82**(5), 2775–2783 (2002).
13. P. M. Hansen, V. K. Bhatia, N. Harrit, and L. Oddershede, "Expanding the optical trapping range of gold nanoparticles," Nano Lett. **5**(10), 1937–1942 (2005).
14. V. Heinrich, W. P. Wong, K. Halvorsen, and E. Evans, "Imaging biomolecular interactions by fast three-dimensional tracking of laser-confined carrier particles," Langmuir **24**(4), 1194–1203 (2008).

#185655 - $15.00 USD Received 20 Feb 2013; revised 28 Mar 2013; accepted 31 Mar 2013; published 9 Apr 2013

15. S. L. Eichmann, S. G. Anekal, and M. A. Bevan, "Electrostatically confined nanoparticle interactions and dynamics," Langmuir **24**(3), 714–721 (2008).
16. S. H. Lee and D. G. Grier, "Holographic microscopy of holographically trapped three-dimensional structures," Opt. Express **15**(4), 1505–1512 (2007).
17. A. Sato, Q. D. Pham, S. Hasegawa, and Y. Hayasaki, "Three-dimensional subpixel estimation in holographic position measurement of an optically trapped nanoparticle," Appl. Opt. **52**(1), A216–A222 (2013).
18. S. R. P. Pavani, A. Greengard, and R. Piestun, "Three-dimensional localization with nanometer accuracy using a detector-limited double-helix point spread function system," Appl. Phys. Lett. **95**(2), 021103 (2009).
19. M. A. Thompson, J. M. Casolari, M. Badieirostami, P. O. Brown, and W. E. Moerner, "Three-dimensional tracking of single mRNA particles in Saccharomyces cerevisiae using a double-helix point spread function," Proc. Natl. Acad. Sci. U.S.A. **107**(42), 17864–17871 (2010).
20. M. Speidel, A. Jonás, and E. L. Florin, "Three-dimensional tracking of fluorescent nanoparticles with subnanometer precision by use of off-focus imaging," Opt. Lett. **28**(2), 69–71 (2003).
21. Z. P. Zhang and C. H. Menq, "Three-dimensional particle tracking with subnanometer resolution using off-focus images," Appl. Opt. **47**(13), 2361–2370 (2008).
22. Y. Park, G. Popescu, K. Badizadegan, R. R. Dasari, and M. S. Feld, "Fresnel particle tracing in three dimensions using diffraction phase microscopy," Opt. Lett. **32**(7), 811–813 (2007).
23. S. Jin, P. M. Haggie, and A. S. Verkman, "Single-particle tracking of membrane protein diffusion in a potential: Simulation, detection, and application to confined diffusion of CFTR Cl- channels," Biophys. J. **93**(3), 1079–1088 (2007).
24. W. P. Wong and K. Halvorsen, "The effect of integration time on fluctuation measurements: calibrating an optical trap in the presence of motion blur," Opt. Express **14**(25), 12517–12531 (2006).
25. V. Jacobsen, E. Klotzsch, and V. Sandoghdar, "Interferometric detection and tracking of nanoparticles," in *Nano Biophotonics: Science and Technology*, H. Masuhara, S. Kawata, and F. Tokunaga, eds. (Elsevier, 2007).
26. K. Lindfors, T. Kalkbrenner, P. Stoller, and V. Sandoghdar, "Detection and spectroscopy of gold nanoparticles using supercontinuum white light confocal microscopy," Phys. Rev. Lett. **93**(3), 037401 (2004).
27. J. Ortega-Arroyo and P. Kukura, "Interferometric scattering microscopy (iSCAT): new frontiers in ultrafast and ultrasensitive optical microscopy," Phys. Chem. Chem. Phys. **14**(45), 15625–15636 (2012).
28. J. N. Israelachvili, *Intermolecular and Surface Forces* (Academic Press, 2011).
29. M. Krishnan, N. Mojarad, P. Kukura, and V. Sandoghdar, "Geometry-induced electrostatic trapping of nanometric objects in a fluid," Nature **467**(7316), 692–695 (2010).
30. N. Mojarad and M. Krishnan, "Measuring the size and charge of single nanoscale objects in solution using an electrostatic fluidic trap," Nat. Nanotechnol. **7**(7), 448–452 (2012).
31. P. Kukura, H. Ewers, C. Müller, A. Renn, A. Helenius, and V. Sandoghdar, "High-speed nanoscopic tracking of the position and orientation of a single virus," Nat. Methods **6**(12), 923–927 (2009).
32. B. E. A. Saleh and M. C. Teich, *Fundamentals of Photonics* (Wiley Interscience, 2007).
33. M. Meier and A. Wokaun, "Enhanced fields on large metal particles - dynamic depolarization," Opt. Lett. **8**(11), 581–583 (1983).
34. B. Richards and E. Wolf, "Electromagnetic diffraction in optical systems. 2. Structure of the image field in an aplanatic system," Proc. R. Soc. Lon. Ser-A **253**, 358–379 (1959).
35. L. Novotny and B. Hecht, *Principles of Nano-Optics* (Cambridge University, 2006).
36. S. T. Hess and W. W. Webb, "Focal volume optics and experimental artifacts in confocal fluorescence correlation spectroscopy," Biophys. J. **83**(4), 2300–2317 (2002).
37. J. Kerssemakers, L. Ionov, U. Queitsch, S. Luna, H. Hess, and S. Diez, "3D nanometer tracking of motile microtubules on reflective surfaces," Small **5**(15), 1732–1737 (2009).
38. G. G. Daaboul, A. Yurt, X. Zhang, G. M. Hwang, B. B. Goldberg, and M. S. Ünlü, "High-throughput detection and sizing of individual low-index nanoparticles and viruses for pathogen identification," Nano Lett. **10**(11), 4727–4731 (2010).
39. N. M. Mojarad, G. Zumofen, V. Sandoghdar, and M. Agio, "Metal nanoparticles in strongly confined beams: transmission, reflection and absorption," J. Eur. Opt. Soc.- Rapid Publ. **4**, 09014 (2009).
40. T. Savin and P. S. Doyle, "Role of a finite exposure time on measuring an elastic modulus using microrheology," Phys. Rev. E Stat. Nonlin. Soft Matter Phys. **71**(4), 041106 (2005).

1. Introduction

Techniques to measure forces between discrete entities in fluids, ambient air, or vacuum have been vital in advancing our understanding of condensed matter. From the invention of the surface force apparatus (SFA) that permitted early measurements of interactions between macroscopic surfaces [1], followed by atomic force microscopy (AFM) which carried this principle over to micro and nanoscale entities [2], to the more recent use of optically and magnetically trapped microspheres as indirect sensors of forces in macromolecules [3], the development of tools for interaction potential measurements continues to be a vibrant area of research. While the methods listed above rely on the mechanical motion (e.g. bending or

#185655 - $15.00 USD Received 20 Feb 2013; revised 28 Mar 2013; accepted 31 Mar 2013; published 9 Apr 2013

displacement) of a sensing element in response to the action of an intermolecular force, optical microscopy has emerged as a sensitive, non-invasive, and often calibration-free tool, that offers a thermodynamic method to directly measure interaction energies [4]. In particular, it facilitates highly parallel realizations of the measurement. The technique has been successfully used to study a variety of interactions in soft matter: electrostatic interactions of charged colloids, polymers and lipid membranes [5–7] as well as van der Waals [8], gravitational [9], depletion [10] and critical-Casimir [11] forces to name a few.

These measurements are founded in the Boltzmann principle for a system in thermodynamic equilibrium, where the potential ascribed to a state depends exclusively on the probability of occupancy of that state. Thus in colloidal systems, spatially varying interaction potentials may be measured by acquiring a large number of snapshots of a probe particle thermally sampling its surroundings. Normalized probability density distributions of the particle's instantaneous location, $P(r)$ measured in the experiment can be converted to local potentials via the Boltzmann relation, $U(r) = -\ln P(r)$.

Although AFM and SFA provide angstrom spatial resolution and may be ubiquitously applied, optical imaging could deliver better sensitivity in particular experimental situations. In optical imaging, the particle localization accuracy determines the spatial resolution with which the interaction can be measured and this is generally on the order of a nanometer [12]. However since the range of the measurement, especially in the lateral dimension, can be on the order of micrometers, the technique is particularly well suited to measuring potentials that change monotonically and gradually with distance, thus putting fN force measurement within its reach.

Provided that snapshots of the particle can be acquired with a high signal-to-noise ratio (SNR), optical imaging is an excellent calibration-free method for direct mapping of potential landscapes of arbitrary shape and large range. Although quadrant photodiodes (QPDs) offer outstanding temporal resolution, and have been successfully used to calibrate optical traps [13], their position sensitivity is linear over a limited range of displacements (<1 μm), and they cannot be used to track more than one particle at a time. Direct imaging, therefore, offers distinct advantages in parallelized measurements of potentials over an extended spatial range, and can provide full three dimensional (3D) information on an interaction in a single run.

Most imaging-based interaction potential measurements deal with micron-scale objects, which typically permit very high SNR imaging, and with few exceptions [14] concentrate on the measurement of 2D potentials in the imaging plane. Studies that measure potentials in the axial dimension using nanoscale probes are less common and mainly use evanescent excitation at the fluid-glass interface (TIRM) [15]. TIRM is intrinsically constrained by the fact that the local excitation field falls off exponentially from the interface and therefore limits measurements to within ~100 nm of the interface. Other 3D particle tracking methods such as holographic microscopy [16, 17], point-spread function engineering [18, 19], off-focus imaging [20, 21], and Fresnel particle tracking [22] offer the ability to track particle motion over an extended range of axial displacements, however face challenges in supporting nanometer scale positional accuracy combined with >kHz imaging rates, which are required when using nanoscale objects as probes to directly map arbitrarily shaped potential landscapes.

Apart from the SNR, a further subtlety in performing accurate position measurements, on small particles (<100 nm in diameter) in water, relates to the exposure time of the measurement, σ. A particle trapped in a harmonic potential well of spring constant, k has a relaxation time given by $\tau = \gamma / k$, where γ is the viscous drag experienced by the particle. When σ is comparable to the relaxation time τ, the timescale over which the particle experiences net motion towards the bottom of the well, the measured position of the particle is weighted towards the bottom of the potential, making the trap appear stiffer than it really is [23, 24]. Measurement and correction of "motion blur" has been discussed in detail for

#185655 - $15.00 USD Received 20 Feb 2013; revised 28 Mar 2013; accepted 31 Mar 2013; published 9 Apr 2013

harmonic confining potentials that arise in the context of optical trapping [24]. Thus the need arises for an optical imaging technique delivering 3D particle tracking with nanometer spatial and submillisecond temporal resolution.

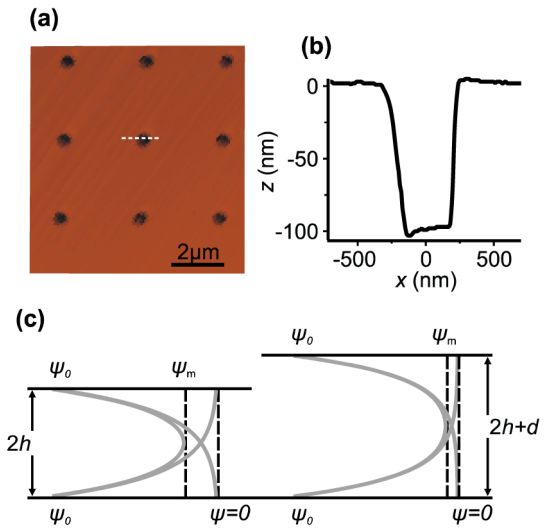

Fig. 1. (a) Atomic force micrograph of an array of 500 nm pockets separated by 3 μm. (b) Line plot of the topography of one pocket indicated in (a). (c) Schematic of the electrostatic potential between two parallel walls separated by a smaller (left) and larger (right) gap.

Here we describe the details of an optical technique, "interferometric scattering" (iSCAT) imaging [25–27] that delivers accurate particle localization in 3D and can in principle be used to reconstruct spatial interaction energy landscapes for nanometer scale particles in 3D. Our experimental measurement addresses the interactions of charged gold particles thermally sampling an electrostatic potential landscape generated in a fluidic slit. In contact with water, the walls of the slit acquire a surface charge comparable to that of the particle. The electrostatic potential near an isolated glass or SiO_2 surface, ψ decays exponentially away from the surface value, ψ_0 as: $\psi(z) = \psi_0 e^{-\kappa z}$, where κ^{-1} is the "Debye length" and for a monovalent electrolyte may be given by $0.304/\sqrt{C}$, where C is the salt concentration in solution expressed in mol/L [28]. Two charged planes separated by a gap $2h$ in a fluid thus give rise to an electrostatic potential minimum midway between them. For low values of ψ_0, the potential at the midplane due to both surfaces can be taken to be simply additive and is given by $\psi_m = 2\psi_0 e^{-\kappa h}$ (Fig. 1(c)). A local increase in the gap width of d would give a local potential minimum of $\psi_m = 2\psi_0 e^{-\kappa(h+d/2)}$. So a point charge q, traversing a width modulation in the gap would experience a change in electrostatic energy given by $\Delta U = 2q\psi_0 e^{-\kappa h}(1-e^{-\kappa d/2})$. When $d \to 0$, i.e., the width modulation vanishes, the slit consists of two flat parallel walls facing each other, and $\Delta U \to 0$. For large κd, on the other hand, $\Delta U = 2q\psi_0 e^{-\kappa h}$. While these simple considerations - based on the linearization of the governing equations valid for low surface potentials or far away from surfaces - are not quantitatively exact, they give a physical picture of how geometrical modulation of a gap can translate to a modulation of the electrostatic potential in a fluid. They also furnish key insight into optimal design of electrostatic landscapes to trap and manipulate single charged particles in fluids. Accordingly, systems with small values of κh and walls with a high surface potential, ψ_0 would be expected to work best in creating deep local potential wells, capable

#185655 - $15.00 USD Received 20 Feb 2013; revised 28 Mar 2013; accepted 31 Mar 2013; published 9 Apr 2013

of retaining a charged object for a long time. Furthermore under a given set of conditions, i.e. ionic strength and slit depth, the shape and depth of each local potential well can be tailored using the geometry of the surface indentation. We have demonstrated stable trapping of charged nanospheres as small as 20 nm polystyrene and 50 nm aqueous lipid vesicles in water [29] and have recently described how spatial mapping of potential wells can be used in conjunction with free energy calculations to directly measure the charge of single trapped objects in a highly parallel fashion [30]. In this work we consider the electrostatic interaction between charged gold particles, 80 nm in diameter, and confining walls, composed of glass and SiO_2 with etched cylindrical indentations, or "pockets" on the top surface, and discuss details on the use of iSCAT imaging to probe in 3D the morphology of potential wells generated by different pocket geometries.

In our scanning focused beam setup [29–31], a collimated laser beam is continuously swept by a two-axis acousto-optic deflector (AOD). In such a system the deflection angle from the propagation axis, *z* corresponds to an *xy* position of the focused diffraction-limited spot in the vicinity of trapped particles. The combination of large scanning bandwidth of each AOD (between 50 and 100 kHz), which results in the rapid scanning of the diffraction-limited spot, and a fast CMOS camera, ensures a uniform illumination area in each frame, acquired over an exposure time of $\sigma = 1\text{ms}$. While faster acquisition is possible using more rapidly scanning AODs, we achieve exposure times down to 200 μs in the current configuration [30], however with a greatly reduced field of view. 1 ms exposure times produce a stable uniform wide-field illumination that we use to study particles trapped by pockets of various geometries. In such a coherent detection scheme, the fields that produce the image at the camera predominantly originate from the field strongly scattered by the trapped nanoparticle at the beam focus and the highly reflecting SiO_2/Si interface. The scanned illumination eliminates undesired interference fringes originating from the light reflected from distant locations and interfaces in the multilayer device.

We further note that in our scanning beam illumination, the particle is sampled approximately 10 times during an exposure time of 1 ms. This may be compared with imaging and tracking the center of mass of a particle during the same exposure time, but with continuous illumination in a static beam. In the latter, light from the particle continuously accumulates on the camera and the fit to the final accumulated intensity distribution gives its average spatial location during the illumination. The use of a static beam that continuously illuminates the particle, or a scanning beam that stroboscopically samples the particle multiple times during in the exposure, primarily changes the accumulated intensity in the image. The "scanned" beam case naturally contains fewer samples than the "static" beam case, but since we acquire ~10 samples with scanning, the average inferred position approximates the continuously illuminated value reasonably well. Finite sampling could however be expected to reduce the effective exposure time compared to the camera exposure time. This difference may be estimated to be σ / s, where *s* is the number of samples, so that as *s* gets larger the values converge. In our experiments we estimate that the sampling rate results in an effective exposure time of 0.9 ms for a $\sigma = 1\text{ms}$ camera exposure. For smaller exposure times, use of a greatly reduced field of view ensures that the illumination as seen by the particle tends to the continuously illuminated case.

#185655 - $15.00 USD Received 20 Feb 2013; revised 28 Mar 2013; accepted 31 Mar 2013; published 9 Apr 2013

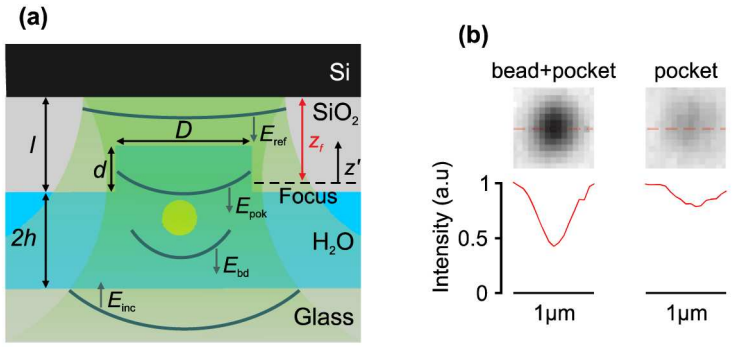

Fig. 2. (a) Schematic of electromagnetic fields involved in forming an iSCAT image in the trapping device. (b) iSCAT image of a trapped 80 nm gold nanoparticle (left) and a D = 500 nm pocket (right). The intensity profile along the dashed line in each image is plotted in the graph below it.

2. Results and discussion

A schematic of our nanofluidic trapping device is shown in Fig. 2(a). We study the effect of three different trap geometries created by cylindrical indentations of diameter D = 100, 200 and 500 nm, of constant depth, d = 100 nm (Fig. 1(b)). The pockets in the SiO_2 were etched in arrays with a spacing of 3 μm (Fig. 1(a)), which facilitated parallel imaging and tracking of several trapped particles. Gold nanoparticles 80 nm in diameter suspended in water at low ionic strength solution, ~0.05mM, were used as test objects, with zeta potential measurements providing an average charge estimate of ~-80e per particle.

iSCAT imaging is based on coherent detection of the interference between elastically scattered light from an object and a reference beam [25, 26, 29]. Figure 2(a) illustrates the optical fields that create an iSCAT image of a trapped object, illuminated by a scanning focused laser beam. In this configuration, the full 3D information on the particle locus is embedded in the interferometric dip in the image due to the beam reflected from the Si/SiO_2 interface, E_{ref} and the field scattered by the trapped particle, E_{bd}. The 3D locus of the particle can be extracted from this signal by fitting a 2D Gaussian function to the spatial intensity distribution in the image. The peak position of the Gaussian fit yields the lateral coordinates of the particle, x and y, while the amplitude of the fit function can be directly related to the axial location, z via a calibration function. The channel depth, $2h$ in the range of 200 to 220nm and SiO_2 thickness, l~200 nm can be used to manipulate the optical path length (OPL) difference between the detected waves and optimize the axial calibration function as described later. We present details of the axial calibration procedure after reviewing the particle trapping results.

As explained earlier, the shape of a potential well may be reconstructed from the measured spatial probability density distribution of a trapped particle, thermally sampling the landscape. Figure 3(a) illustrates scatter plots in the xy plane of representative particles confined in potential wells with different geometries, where each point represents the particle's position at one specific frame. Normalized radial probability density distributions, $P(r)$ from such scatter plots can be used to make quantitative comparisons of experiment with theory [30]. The average radial probability distributions of particles trapped by the three geometries, obtained by tracking an ensemble of objects, is presented in Fig. 3(b). As displayed, the pocket width, D significantly influences both the axial and lateral range of motion of a confined particle. The measured $P(r)$ distribution for a particle trapped by a D = 500 nm pocket reveals a square-well potential with soft walls. Furthermore, the 3D scatter plot of a representative particle (Fig. 3(d)) reveals that not only are particles confined to a much shorter range in the axial dimension (~50 nm) compared to the radial, but that the

#185655 - $15.00 USD Received 20 Feb 2013; revised 28 Mar 2013; accepted 31 Mar 2013; published 9 Apr 2013

scatter plot exhibits a conical shape, reflecting the presence of the indentation overhead. Decreasing D results in stronger spatial confinement in all dimensions. As depicted in Figs. 3(a) and 3(b), the lateral confinement of particles trapped by D = 200nm decreases substantially in comparison with D = 500nm. In particular $P(r)$ in this case has a profile, which is well approximated by a Gaussian function, indicating that the particle is trapped in a harmonic potential; the stiffness of this potential has been shown to strongly depend on the charge of the particle [30].

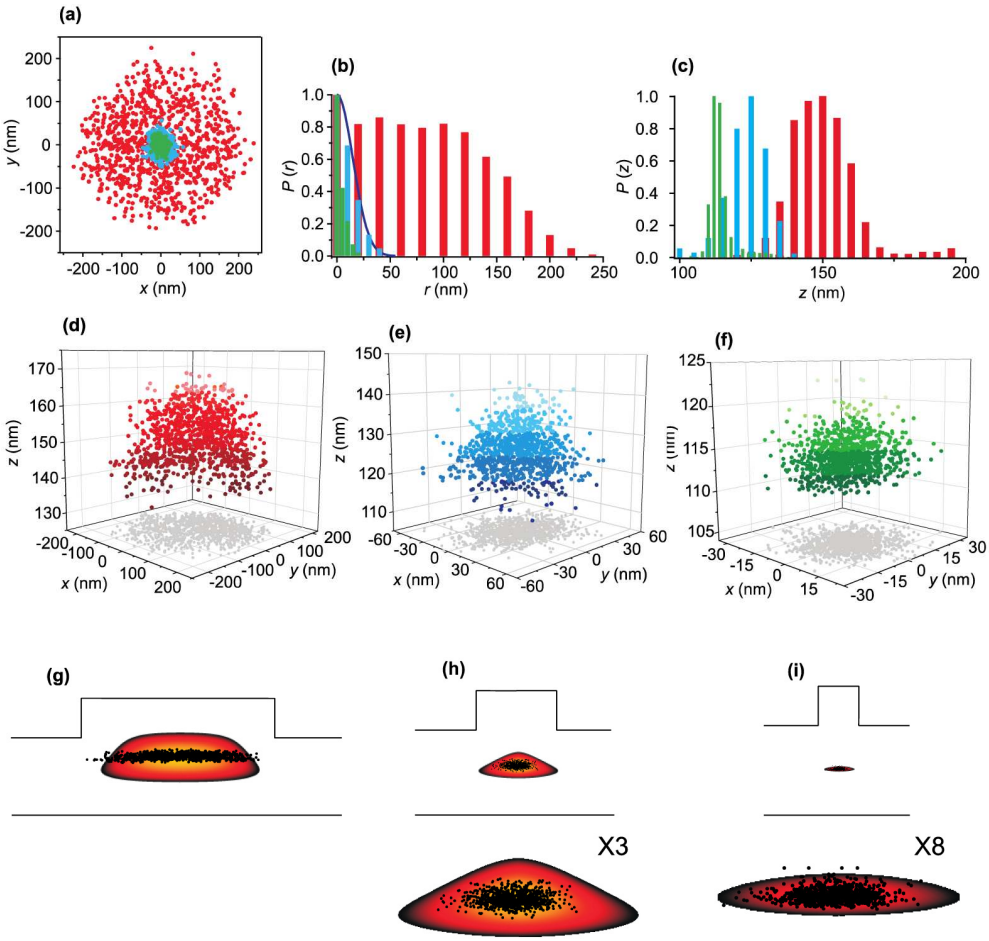

Fig. 3. (a) Scatter plots of lateral motion for representative 80 nm gold particles trapped by D = 500 nm (red), 200 nm (blue), and 100 nm (green) pockets acquired with $\sigma = 1\,\mathrm{ms}$. (b) Averaged radial and (c) axial probability density distributions obtained by tracking an ensemble of particles trapped by the three pocket geometries. (d), (e), (f) 3D scatter plots of representative particles trapped in the three geometries and (g), (h), (i) their overlay on the corresponding calculated electrostatic potential distribution. The panels under (h) and (i) represent the same plots magnified 3 and 8 times respectively. The electrostatic potential is presented on a color scale going from high (black) to low energy (yellow) for a unit negative charge. For emphasis, only the minimum of the well is shown.

In order to make controlled comparisons between our experimental findings and theoretical predictions, we performed numerical calculations of the potential distribution in the trapping nanostructure using COMSOL Multiphysics [29]. Figures 3(g)-3(i) depict the projection of 3D scatter plots of Figs. 3(d)-3(f) in the *xz* plane, overlaid on the calculated

#185655 - $15.00 USD Received 20 Feb 2013; revised 28 Mar 2013; accepted 31 Mar 2013; published 9 Apr 2013

potential distribution. In all three cases, the measured most probable location of a particle coincides with the location of the potential minimum as expected from Boltzmann statistics. As depicted in Fig. 3(c), increasing D not only increases the range of levitation, but the trapped particles also levitate about higher mean axial positions. The midplane of levitation, z_{m}, defined as the average z value over the entire measurement, could thus be used to compare the experimental and theoretical results. Table 1 displays the experimentally measured and calculated values which are in good agreement for all three geometries considered.

Table 1. Geometrical parameters of the devices and predicted and ensemble-averaged measured midplanes of levitation. All units are in nanometers.

Pocket width, D	100	200	500
Chanel depth, $2h$	220	215	200
SiO_2 thickness, l	177	170	197
Theoretical midplane	110	123	150
Measured midplane, z_{m}	114.3 ± 1.6	125.8 ± 2.6	150.6 ± 2.4
Focus to reflecting interface, z_{f}	200	170	180

3. Method of 3D iSCAT

In the present coherent imaging scheme, the signal at the detector, I_{d} consists of the interference of fields scattered by the trapped bead, E_{bd}, the trapping nanostructure or pocket overhead, E_{pok}, and the field reflected from the Si/SiO_2 interface, E_{ref} (Fig. 2(a)). In analyzing the overall interference, the vectorial nature of the fields is ignored while the phase is taken into account. In our experiments E_{bd} and E_{pok} have the same order of magnitude and are small in comparison to E_{ref}, due to the strong reflection of the SiO_2/Si interface near the beam focus. As a result, the pure scattering terms, $\left|E_{\mathrm{bd}}\right|^2$ and $\left|E_{\mathrm{pok}}\right|^2$ can be omitted and the detected signal consists of a constant background, $\left|E_{\mathrm{ref}}\right|^2$ and the interference of E_{bd} and E_{pok} with E_{ref}. I_{d} could therefore be written as:

$$I_{\mathrm{d}} = \left|E_{\mathrm{ref}} + E_{\mathrm{bd}} + E_{\mathrm{pok}}\right|^2 \approx \left|E_{\mathrm{ref}}\right|^2 + 2\,\mathrm{Re}\left\{E_{\mathrm{ref}} \cdot E_{\mathrm{bd}}^*\right\} + 2\,\mathrm{Re}\left\{E_{\mathrm{ref}} \cdot E_{\mathrm{pok}}^*\right\}. \qquad (1)$$

Note we ignore the interference term consisting of $E_{\mathrm{bd}} \cdot E_{\mathrm{pok}}^*$ as it is negligible in comparison with terms containing E_{ref}. The effect of the two remaining interference terms can be seen in Fig. 2(b). As illustrated, the detected signals appear as dark regions over a uniform, bright background, indicating that the interference terms indeed dominate pure scattering from the particle, $\left|E_{\mathrm{bd}}\right|^2$. Moreover, the interference signal in the image actually consists of contributions from both the particle and the pocket and is larger than that of an "unoccupied" trapping pocket. All intensities are defined as the imaged contrast; that is, the ratio of the detected dip over the constant background, which is set to 1. Since $E_{\mathrm{ref}} \cdot E_{\mathrm{bd}}^*$ contains the spatial location information of the trapped bead, we subtract the interference contribution of the trapping pocket, $2\,\mathrm{Re}\left\{E_{\mathrm{ref}} \cdot E_{\mathrm{pok}}^*\right\}$, from each frame of the acquired image series. This is

#185655 - $15.00 USD Received 20 Feb 2013; revised 28 Mar 2013; accepted 31 Mar 2013; published 9 Apr 2013

done by generating an image of a pocket with the same parameters (Gaussian width and amplitude) as the experimentally recorded image of a particle-free pocket. The center of the pocket in this image is set to coincide with the center-of-mass of motion of the particle in the raw image stack. Subtracting the pocket image from the raw stack yields background-free images of the particle that may be analyzed further.

Full 3D motion of the particle is obtained by fitting a 2D Gaussian function to the intensity distribution in each frame. The axial location of the particle, z directly correlates with the amplitude of the fit, $I(z)$. The magnitude of $I(z)$ results from the far-field interference of E_{ref} and E_{bd}, which varies with a changing OPL difference between these waves. Consider the propagation of the two waves (Fig. 2(a)) based on the device geometry. For a particle levitating at a height z the measured intensity may be written as follows:

$$I(z) = I_0 \cos\left[2k_{\mathrm{w}}(2h+d) + 2k_{\mathrm{s}}(l-d) - 2k_{\mathrm{w}}z + \varphi_{\mathrm{sys}}\right]. \quad (2)$$

In this equation k_{w} and k_{s} are the wave numbers in water and SiO_2 respectively, and together with h, d and l are the known parameters. φ_{sys} is a systematic phase that contains contributions from three effects, namely the Gouy phase accumulation by E_{inc} and E_{ref} [32], the phase added to the incident field upon reflection at the Si/SiO_2 interface, and the retardation phase of the particle due to the complex permittivity of gold [33]. In Eq. (2), the amplitude, I_0 and φ_{sys} are two unknown parameters that may, however, be determined by recording the intensities of particles located at known values of z. As illustrated in Fig. 4(c), we measured the contrast of several particles stuck at the water/SiO_2 interface and took the mean of these values as representing the contrast of the average-sized particle located at $z_1 = 2h - a$ (a is the radius of a gold particle). These particles randomly immobilized at the water/glass and water/SiO_2 surfaces most likely due to attractive van der Waals forces. For this case the contrast maybe written as:

$$I(z_1) = I_0 \cos\left(4k_{\mathrm{w}}h + 2k_{\mathrm{s}}l - 2k_{\mathrm{w}}z_1 + \varphi_{\mathrm{sys}}\right). \quad (3)$$

The mean contrast of particles stuck at the top surface of another slit etched $\delta l = 30\mathrm{nm}$ deeper into the SiO_2, gives an additional equation for $I(z_2)$ thus enabling us to determine the two unknowns, I_0 and φ_{sys}. Further details on this procedure are described below.

We point out that while the highly reflective Si/SiO_2 interface facilitates iSCAT measurements on strongly scattering particles, the intense reflection also results in an axially non-uniform excitation field in the vicinity of the particle, having the form of a partial standing wave. As a result, I_0 in Eq. (2) is not a constant but itself depends on z, altering the effective calibration function for particle contrast. We account for this modulation by mathematically modelling a focused beam reflected at a water/Si interface by first, decomposing E_{inc} into plane waves propagating in all directions within the angular spectrum [34]. The field reflected from the interface, E_{ref} is consequently found by multiplying the amplitude of each incident plane wave by the corresponding Fresnel reflection coefficient [35]. The total local field experienced by the illuminated particle is obtained by the superposition of E_{inc} and E_{ref}. To model E_{inc} we considered the experimental parameters that were used, namely, a 1.4NA oil-immersion objective with an underfilling fraction of ~70%, associated with the incident Gaussian beam partially covering the back aperture of the microscope objective [36]. The maximum focusing angle was set by the total internal reflection of the beam at the glass/water interface (62°). We emphasize that although the calculation of the local electric field assumes that the beam propagates through water, the

#185655 - $15.00 USD Received 20 Feb 2013; revised 28 Mar 2013; accepted 31 Mar 2013; published 9 Apr 2013

SiO_2 layer is taken into consideration in the OPL differences in Eq. (2). Figure 4(a) shows a 2D contour plot of the total illumination intensity in the vicinity of the Si/SiO_2 interface on a logarithmic scale. In Fig. 4(b) the normalized on-axis variation of the total intensity can be compared in the presence and absence of the Si/SiO_2 interface reflection. Clearly, the reflection produces a significant axial modulation in the field experienced by the particle, similar to the standing wave excitation in Fluorescence Interference Contrast (FLIC) microscopy [37].

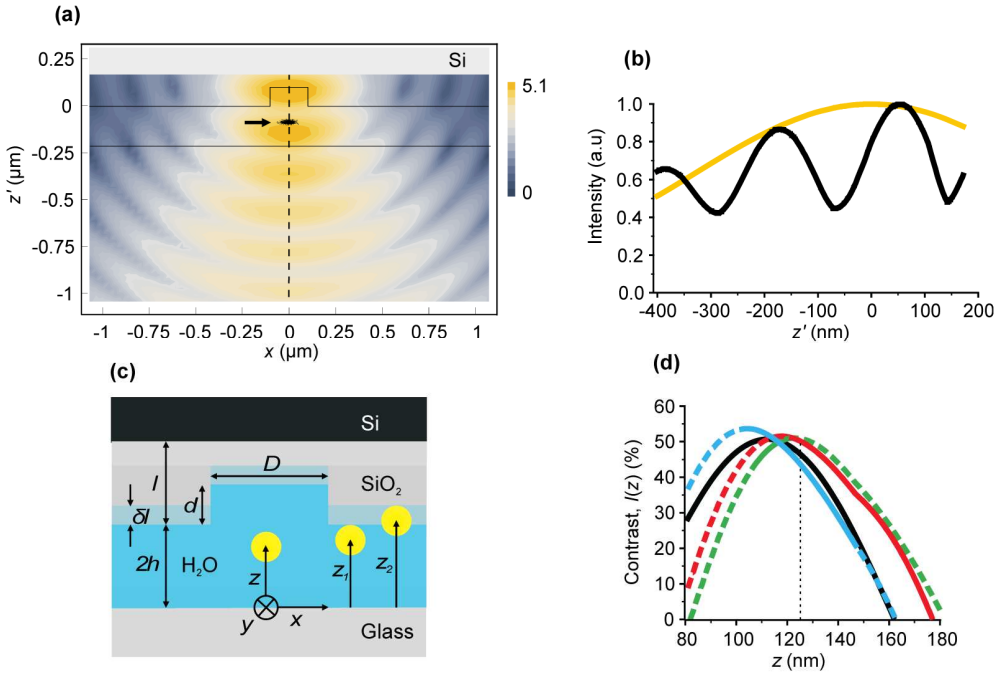

Fig. 4. (a) Calculated electromagnetic field intensity (in logarithmic scale) of a focused Gaussian beam propagating in water and reflecting off a Si surface 170 nm away from the focus. The intensity scale bar indicates the intensity in logarithmic scale, the solid lines show the geometry of the D = 200nm trapping pocket in a slit of depth d = 215 nm and the points highlighted by the arrow represent the scatter plot displayed in Fig. 3(h). (b) The black line is the axial profile of the total intensity in (a) along $x = 0$ indicated by the dashed line. z' is the axial distance from the beam focus. The yellow line is the intensity in the absence of the reflected field. (c) Schematic drawing of the particles attached to the SiO_2/H_2O interface used to determine the calibration function for axial motion. (d) Curves used to calibrate the motion of particles trapped by D = 500 nm (red), 200 nm (blue), and 100 nm (green) pockets. The solid segments of each curve represent the axial range sampled by corresponding levitating particles. The black line represents the calibration curve for trapping by the D = 200 nm pocket, when not taking the standing wave effect into account.

The axial excitation profile further depends on the distance z_f of the beam focus from the Si/SiO_2 interface and was calculated for different values of z_f; we denote the calculated profile as $I_0(z, z_f)$. Since we do not have a direct measurement of z_f, we determined it in an indirect fashion as follows. We used the same focusing criterion in all experiments: the axial location of the device relative to the microscope objective was adjusted using a piezo-mounted stage to ensure that a D = 500 nm pocket displayed maximum contrast. We performed trapping experiments on particles using pockets of different diameters in devices with different values of l and $2h$, and found the maximum experimentally obtainable value of particle contrast, I_{max}. We then used the intensity and position data of the calibration particles

#185655 - $15.00 USD Received 20 Feb 2013; revised 28 Mar 2013; accepted 31 Mar 2013; published 9 Apr 2013

$I(z_1)$ and $I(z_2)$ and a function representing the theoretical axial excitation profile $I_0(z, z_f)$ in Eq. (2) to determine the maximum expected particle contrast I_{max} and system phase, φ_{sys} for a given device configuration. Agreement between I_{max} and $I_0(z, z_f)$ was taken as a criterion to determine the value of z_f and hence the calibration curve for that device. Small changes in z_f from the determined value in each case gave $I_0(z, z_f)$ magnitudes larger or smaller than the experimentally observed I_{max}. For example for the case shown in Fig. 3(e), an increase in z_f from 170 to 180 nm would increase $I_0(z, z_f)$ by 17% and also shift the measured mean levitation plane by + 5 nm. z_f is thus a fit parameter in the axial calibration and its value for various device configurations lies in a fairly tight range between 170 and 200 nm. Figure 4(d) shows the axial calibration curves obtained for the three different device configurations that were used in the experiments. The solid sections of the curves show the range of axial displacements sampled by the particles. Comparing calibration curves for the *D* = 200nm case including the reflection (blue) and excluding it (black) demonstrates that the standing wave mainly alters the amplitude of the expected particle contrast, but also slightly shifts the location of this peak. Accurate measurements of the axial motion can be obtained over half a period of Eq. (2), where the signal varies from maximally bright to dark, which corresponds to ~100nm in these experiments. In the trap geometries and imaging conditions we explored, particles levitate over a range <50nm, a distance over which the contrast is expected to change from 0 to I_{max}, thus permitting accurate axial localization. In such an experiment the OPL in Eq. (2) may be optimized by choosing values of *l* and 2*h* to ensure that *I* depends monotonically on *z*. As the slit depth 2*h* is, in fact, a trap parameter, altering it also influences the levitation midplane as well as the range of motion of the trapped particle. An increase in slit depth of δl for example, effectively shifts z_m by $\sim \delta l / 2$. Manipulating these thicknesses, therefore, enables us to shift the calibration function and levitation plane of the particle relative to each other in order to ensure that the range of particle's axial motion is contained within a monotonic segment of the calibration function.

In our iSCAT imaging scheme, the high SNR and sensitivity to the axial motion enables very accurate particle tracking. Figure 5 illustrates the transverse (δx) and axial (δz) localization precisions as a function of the particle contrast. δx monotonically decreases as the signal increases [12]. In the case of particles trapped by *D* = 500 nm pockets, the contrast varies from nearly zero to almost I_{max}, which accordingly corresponds to an average 2.5 nm lateral localization precision and an axial localization precision in the range 0.18 - 1.61 nm, with an average of 0.32nm. δz is obtained by considering the uncertainty in determining the amplitude of the Gaussian fit function (δI) according to $\delta z = |\partial z / \partial I| \delta I$. As shown in Fig. 5, the localization precision at low contrasts is subnanometric and it monotonically increases with contrast. Although δI is smaller for images with higher contrast, when $I \to I_0$ the derivative of the above equation rapidly increases. In summary, for a given range of axial motion the OPLs may be adjusted to optimize the axial resolution over the entire measurement.

#185655 - $15.00 USD Received 20 Feb 2013; revised 28 Mar 2013; accepted 31 Mar 2013; published 9 Apr 2013

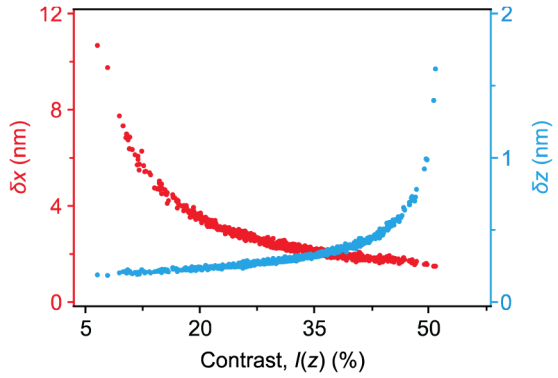

Fig. 5. Measured lateral (red) and axial (blue) localization precision dependence on the contrast of 80nm particles trapped by a D = 500 nm pocket.

We note that the two calibration intensities $I(z_1)$ and $I(z_2)$ were obtained by averaging the intensities of several particles at the SiO_2/H_2O interface. As a result, Eq. (2) applies for particles of the canonical average size. Since the amount of light scattered by a particle depends strongly on its size [26], the measured average values of $I(z)$ on single particles, denoted as I_m, should reflect the size dispersion in the sample. Further, the mean of these I_m values for an ensemble of trapped particles corresponds to the contrast of the canonical trapped particle with the average size. Thus for each trapped particle, the axial calibration was carried out by normalizing the two values of $I(z_1)$ and $I(z_2)$ by m_c, the ratio of I_m of a given particle to the mean contrast of all trapped particles ($m_c = 1$ corresponds to an 80nm particle), and then proceeding with the axial calibration procedure as described previously.

Interestingly, as illustrated in Fig. 6, the measured values of I_m may be further used to estimate the size of the individual trapped particles [38]. The first step in this regard is to use the generalized Mie theory for a spherical particle in a focused beam [39] in order to calculate E_{inc} and E_{bd}, and consequently m_s^2, the ratio of the total scattered power (P_{bd}) to the incident power (P_{inc}), as a function of the particle size. Since both I_m and m_s are proportional to the iSCAT signal, the calculated functional dependence of m_s may be used to directly relate, I_m obtained from the measured optical signal to the particle size. To do this, we set the calculated value of m_s for an 80nm particle to correspond to the average experimentally measured contrast of all trapped particles i.e., to the particle with $m_c = 1$. The estimated sizes of all other trapped particles can then be read off the graph based on their m_c values. Based on this analysis we estimate a particle size dispersion of 9% in the sample, which is in good agreement with the value of 8% quoted by the manufacturer.

#185655 - $15.00 USD Received 20 Feb 2013; revised 28 Mar 2013; accepted 31 Mar 2013; published 9 Apr 2013

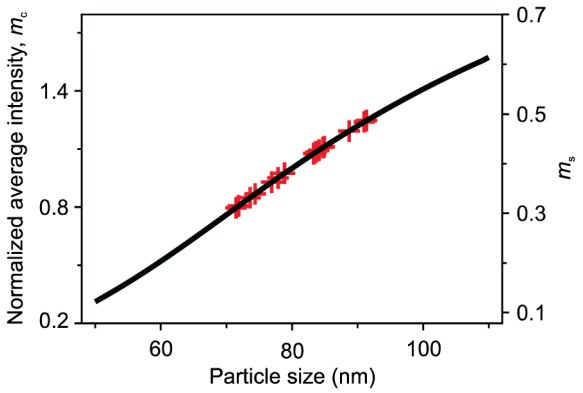

Fig. 6. Calculated dependence of m_s on particle size (black curve) and size estimates of 18 gold nanoparticles trapped by $D = 200$ nm pockets.

4. Conclusion

In our experiment, for a gold bead of diameter 80 nm trapped in a D = 200 nm pocket, calculations show that the bottom of the trap ($r < 60$ nm) is well described by a harmonic potential over a wide range of particle charge. A spring constant of confinement of say 7.5 × 10^{-3} pN/nm, easily achieved for particles under consideration, corresponds to a relaxation time, τ of around 100 μs. Using the attainment of saturation in the plateau values of the mean square displacement with decreasing exposure time as a criterion [40], it is apparent that $\sigma \ll \tau$ is required in order to directly map a potential landscape in a measurement with a single exposure time. In shot-noise limited imaging, a reduction in exposure time by a factor n leads to a localization accuracy poorer by $\sqrt{n}$ [12]. Since a technique like iSCAT is based on elastic scattering of the incident field, a reduction in exposure time can be simply compensated by an increase in excitation power, thereby maintaining the same SNR ratio in each image and in theory permitting access to arbitrarily small exposure times. Our combination of device structure and optical set-up currently permits reliable imaging and tracking using iSCAT down to exposure times of $\sigma = 200$ μs.

Since the average measured position of the particle in a symmetric potential well should coincide with the bottom of the well regardless of the exposure time, and the bottom of the trap in our experiments is harmonic in the axial dimension in all cases (Fig. 3(c)), we find indeed that the axial potential minimum z_m may be nonetheless located accurately independent of exposure time considerations. Furthermore, while we have shown that for harmonic interaction potentials it is indeed possible to reconstruct the true free energy landscape using $\sigma \geq \tau$ [30], rapid (>10 kHz), high SNR imaging techniques would foster direct measurements of arbitrarily-shaped interaction potentials using nanoscale probes.

Acknowledgments

This research work was performed in the Nano-Optics Group at the Laboratory of Physical Chemistry at ETH Zurich before the authors moved to their current institutions. We acknowledge funding from ETH Zurich, Swiss National Science Foundation and a Marie-Curie Fellowship of the European Commission.